Published in "Science 335: 1096, 2012"
which should be cited to refer to this work.

1 Plant material and growth conditions

The wild type tomato cultivar Moneymaker (Wyss, Zuchwil, Switzerland), pDR5rev::3xVENUS-N7 (32), and pAt-PIN1::PIN1:GFP (33) lines were grown in long day conditions (16 h light per day, 110 μEm^2s^{-1}), in $65 \pm 10\%$ humidity, at $20 \pm 2°C$. For in vitro growth assaies 11 days old plants were dissected, apices were transferred on a medium (12), stained with 0.1 % propidium iodide (PI) (Sigma) for 5 min and imaged at 11 h intervals using a confocal microscope.

2 Osmotic treatment

Osmotic treatment was done using mannitol or NaCl water solutions. Apices were plasmolyzed with 0.4 M osmotically active molecule solution and inflated with pure water. 0.2 M solution was used as an estimate for the conditions where they would neither shrink nor swell. For each experiment the apices were first dissected, stained in 0.1 % PI (diluted in 0.2 M mannitol or 0.1 M NaCl) for 5 min and adjusted in 0.2 M mannitol or 0.1 M NaCl for 20 min before the first confocal scan. Next the samples were submerged in hypo-osmotic (0 M) or hyper-osmotic (0.4 M mannitol or 0.2 M NaCl) solutions for 1-2 hours and a second confocal stack was collected. Some of the water treated apices were then exposed to a hyper-osmotic solution for additional 1-2 hours and imaged again to collect data of cell expansion/shrinkage on the same meristem. To check the reversibility of cell size change after hypo-osmotic swelling, several samples were treated for additional 1-2 h with 0.2 M mannitol or 0.1 M NaCl solution and imaged again. At the end of each osmotic treatment, samples were re-stained with 0.1 % PI diluted in a solution of appropriate osmolarity for additional 1 min.

2.1 Determination of plasmolysis point.

Apices were stained with 0.1g/L FM4-64 for 15min and then immersed in 0, 0.1, 0.2, 0.3, 0.4, or 0.5M mannitol for 1hr. At 0.4M we saw cell membranes pulling away from the wall whereas at 0.3M we did not. From this we conclude that cells plasmolyse somewhere between 0.3M and 0.4M. In order to exploit the maximum range of measurement in our osmotic treatments, 0.4M was used for deflation assays.

2.2 Confocal microscopy.

Confocal imaging was performed on a Leica SP5 up-right confocal microscope equipped with a long working-distance water immersion objective (HCX APO L UV-I 63.0 x 0.90 W) and an argon laser emitting at the wavelength of 488nm (Leica Microsystems, Wetzlar, Germany). Images were collected at 500-540 nm for GFP, 505-545 nm for Venus, 600-665 nm for PI, 600-660 nm for FM4-64, and 665-800 nm for chlorophyll autofluorescence. The following scanning setting were used: pinhole size 0.8-1AE, 1x zoom, 20 % laser power, 30 % laser output for the growth assay and 50 % laser output for the osmotic treatment assay, scanning speed of 400 Hz, frame averaging 4, Z intervals of 0.5 μm. Data were collected as 8 or 16 bit images and analysed in MorphoGraphX.

2.3 MorphoGraphX analysis.

Cell segmentation and curvature analysis were performed in MorphoGraphX (34). For segmentation the surface geometry was first extracted from PI or autofluorescence channel, using a marching-cubes algorithm (35). Afterwards a fine subdivision of the surface mesh to more than 300,000 vertices was performed, corresponding to approximately 1000 vertices per segmented cell. A portion of the signal of PI channel (1.5-6 μm from the surface) was then projected onto the resulting curved surface, giving a projection of a curved slice of the data to reveal the cell borders. The surface was segmented into cells using the watershed technique, which was adapted for use on a curved surface mesh. Surface area for individual cells was calculated by summing the several thousand triangles belonging to each cell. This allows surface curvature within each cell to be taken into account in the area calculation. Corresponding cells in corresponding images were co-identified, and heat maps were created for cell size change. Total changes in surface area were also computed. Maps of surface Gaussian curvature were generated for all meristems. Gaussian curvature was assigned for each vertex of a coarse mesh of the surface (around 15,000 vertices), computing the principal curvatures for a neighborhood of around 18μm. To compare expansion in the slow growing region of the meristem tip with surrounding tissue, we chose a tight group of approximately 90 cells on 3 different meristems. Cells that did not belong to the tip region nor boundaries (negative Gaussian curvature) nor primordia were included in the peripheral region.

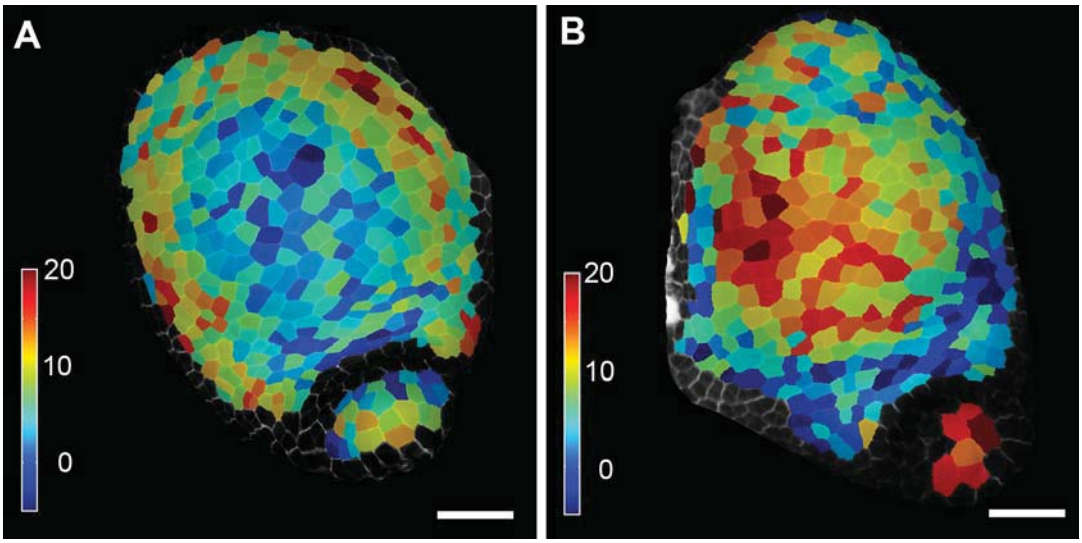

Fig. S1: **Inflation and deflation upon osmotic treatment using mannitol.** (A) Heat map of cell expansion after hypo-osmotic treatment. Note that expansion is lower in the central region and higher in the peripheral region. (B) Heat map of shrinkage after hyper-osmotic treatment. Shrinkage is larger in the central region. Scale bars: 40 μm.

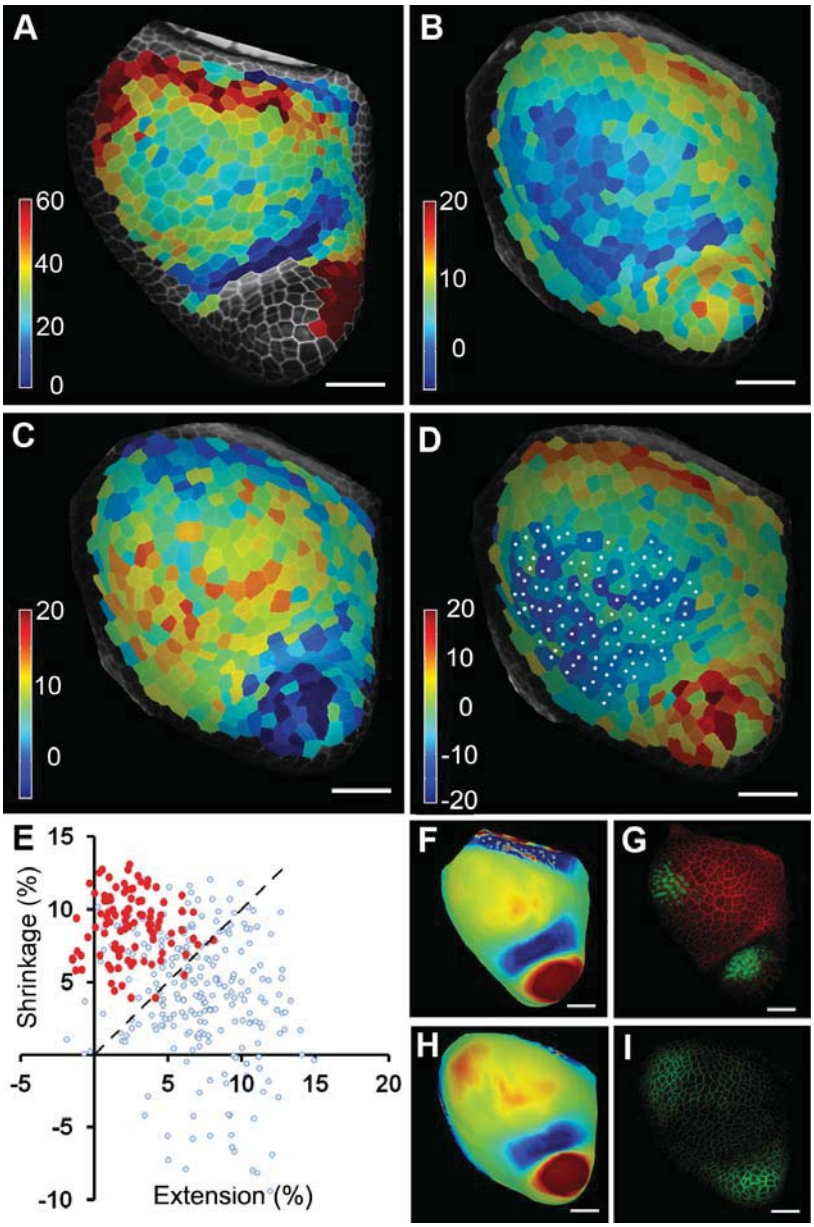

Fig. S2: **Comparison between domains of growth and inflation-deflation upon osmotic treatment.** (A) Heat maps of relative surface area increase over 11h of growth. (B-D) Sequential hypo- to hyper-osmotic treatment using NaCl. (B) Heat map of relative cell surface area expansion after hypo-osmotic treatment. Note that expansion is lower in the central region and higher in the peripheral region, especially in areas expected to be rapidly growing. (C) Heat map of relative cell surface area decrease after hyper-osmotic treatment of the same meristem showing a larger decrease in the central region. (D) Heat map of strain stiffening calculated as percent inflation minus deflation. Cells with lower values (blue) are more strain stiffened. White dots indicate selected cells corresponding to the slow growing region at the apex tip. Apex is at a similar stage as in (A). (E) Scattergraph representing the relative surface areal expansion vs shrinkage in percent for each cell of the osmotically treated apex. Cells colored in red are indicated with white dots in (D). Dashed line is the boundary where cells shrink as much as they expand. (F-H) Gaussian curvature and (G-I) PI signal (red) combined with pDR5::VENUS expression (green) in the epidermis of the apex used for the growth assay (F-G) or for osmotic treatment. The apex used for the growth assay (A, F, G) is in a similar stage of development as the one illustrating inflation-deflation patterns after osmotic treatment (B-D, H, I). Gaussian curvature was used to compare stages of development between apices with the pDR5::VENUS or pPIN1::PIN1:GFP signal marking the youngest primordia. Colorbar (A-D): relative surface area increase or decrease in percent. Color in (F, H) represents Gaussian curvature of the apex surface with red-positive, and blue-negative. Scale bars: 40 μm.

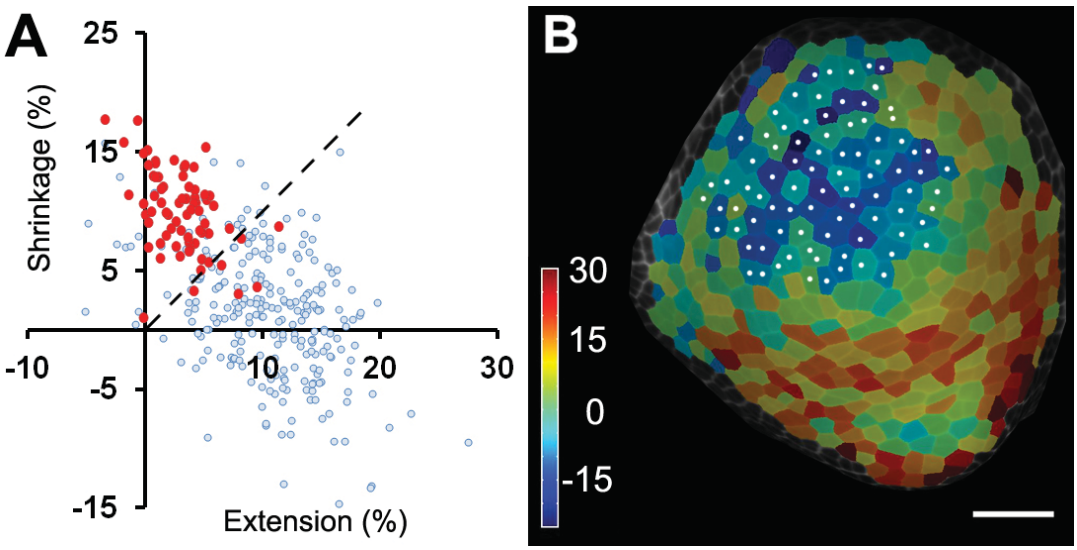

Fig. S3: **Cell strain stiffening.** (A) Scattergraph representing the relative surface areal expansion vs shrinkage in percent for each cell of the osmotically treated apex. Cells colored in red are indicated with white dots in (B). Dashed line is the boundary where cells shrink as much as they expand. (B) Heat map of strain stiffening calculated as percent inflation minus deflation. Cells with lower values (blue) are more strain stiffened. White dots indicate selected cells corresponding to the slow growing region at the apex tip.

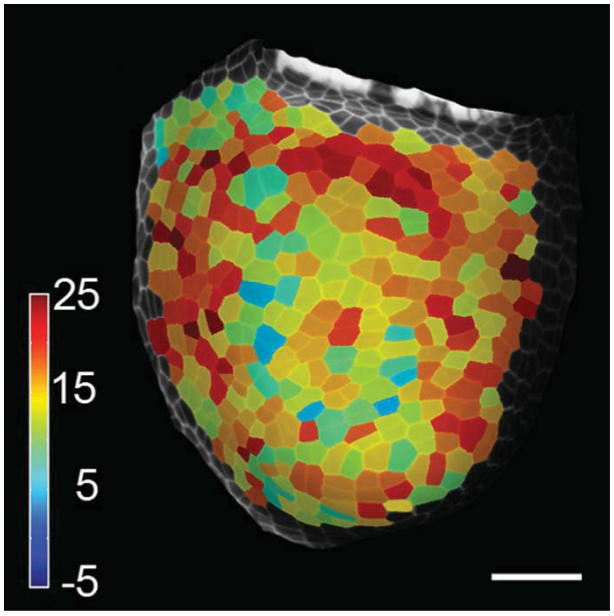

Fig. S4: **Combined map of shrinkage going from hypo- to hyper-osmotic conditions.** The apex is the same as the one shown in figure 3. Notice that the apex central part shrinks less than the flank. Colorbar: relative surface area increase or decrease in percent. Scale bar: 40 μm.

2.4 Error estimate for the segmentation procedure

To estimate the error of cell segmentation in MorphographX, the same shoot apex was imaged with the confocal multiple times after adapting it to 0.2 M mannitol for 30 min. The apex was imaged 2 times and then tilted by approximately 30 degrees and imaged for a third time (Fig. S5). After segmentation, individual cell areas were measured and compared between different scans. Mean relative cell surface area changes in percent were: $1.7 \pm 1.3\%$ (n=320) between first and second scan and $1.8 \pm 1.4\%$ (n=320) between first and last scan. Difference in total surface area was less than 1% in both cases.

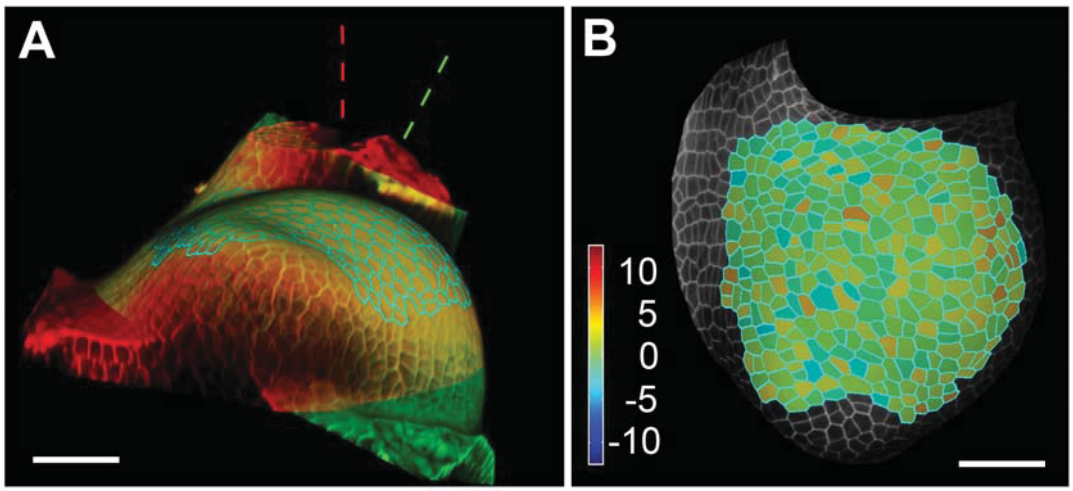

Fig. S5: **Segmentation error estimate.** (A) Overlay of sample imaged twice with the view angle tilted by approximately 30 degrees. Dashed lines indicate the orientation of the Z axis for each stack. Outlined cells were segmented on both stacks and compared. (B) Heatmap of cell size differences is random, and does not show any trends related to surface angle, with the average error per cell less than 2%. Colorbar: relative surface area increase in percent. Scale bars: 40 μm.

3 Quantification of cell wall thickness

For TEM apices were processed as described previously (36) and imaged using a Philips CM 100 BIOTWIN electron microscope. TEM images were used for quantification of cell wall thickness with ImageJ's line tool (http://rsbweb.nih.gov/ij/). Five thinnest regions were quantified per cell face, and the smallest measurement was used to calculate the average ratio between the outermost cell wall to the cell wall between two internal in five independent samples Fig. S6.

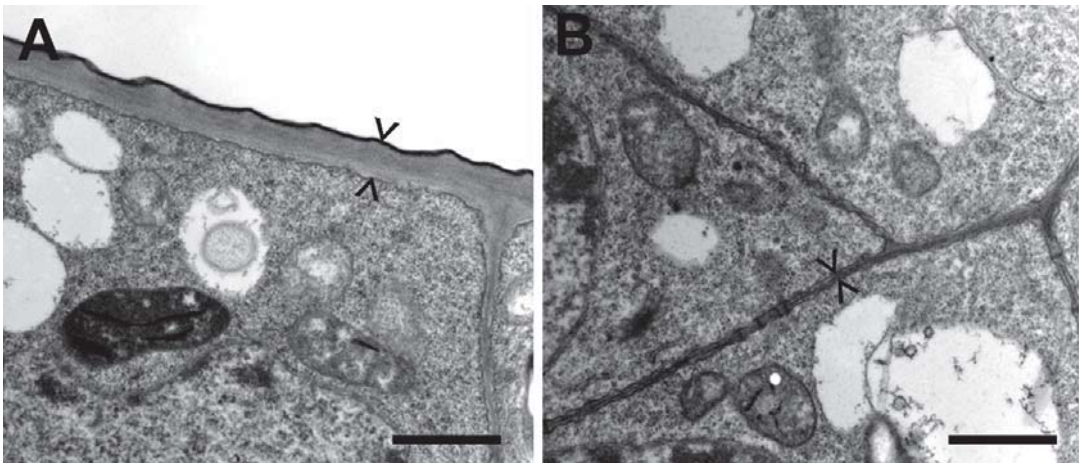

Fig. S6: **Cell wall thickness of the shoot apex.** TEM micrographs of cells in the tomato shoot apicies. (A) Outer cell wall and (B) Inner cell walls. The outer cell wall is (approximately 7 times) thicker than inner cell walls. Arrows point to the cell wall. Scale bars: 1 μm.

4 Mechanical modeling

All mechanical models are based on large-deformation elasticity theory. The simulations were performed using the finite element analysis software Abaqus Standard (http://www.simulia.com/).

4.1 Classification of elastic behavior

For the classification of elastic material models we refer to (37). A material model is called hyperelastic when the relation between stress and strain is derived from a strain energy potential,

$$\sigma_{ij} = \frac{\partial f(\epsilon_{ij})}{\partial \epsilon_{ij}}$$

and linear if it can be written as

$$\sigma_{ij} = d_{ijkl}\epsilon_{kl},$$

where d_{ijkl} is a fourth-order stiffness tensor. Since there are different possibilities for the choice of a strain measure we state more precisely that we mean true (i.e. logarithmic) strain if we call a material model linear.

4.2 Modeling the shoot apex as a hemispherical shell

A commonly used abstraction for plant tissues at the organ level is the shell model (23-27). In this model mechanical stress is thought to be borne mainly by the surface layer of cells. This abstraction is supported by experiments showing that the inner tissue is under compression, with the surface layer under tension (38, 39). This condition would transfer considerable load onto the outer layer(s) of cells.

We used Abaqus to create an axisymmetric shell of constant thickness (0.6 μm) with the shape of a hemisphere (radius 60 μm). The shell was partitioned into two homogeneous sections at a 45 degree angle with respect to the origin. The mechanical behavior of both sections was simulated by using Ogden hyperelastic material models (40). This type of constitutive law is characterized by a polynomial relationship between principal stretch ratios $\lambda_1, \lambda_2, \lambda_3$ and the strain energy density function $W(.)$ which reads as,

$$W(\lambda_1, \lambda_2, \lambda_3) = \sum_{i=1}^{N} \frac{\mu_i}{\alpha_i} (\lambda_1^{\alpha_i} + \lambda_2^{\alpha_i} + \lambda_3^{\alpha_i} - 3)$$

where μ_i, α_i are constitutive parameters. We further imposed the incompressability of materials,

$$\lambda_1 \cdot \lambda_2 \cdot \lambda_3 = 1.$$

For the simulations shown in Fig. 4D-E we chose parameters ($\alpha_1 = 1$, $\mu_1 = 1740$, $\alpha_2 = 2$, $\mu_2 = -1705$, $\alpha_3 = 300$, $\mu_3 = 4.173e-7$) for the apex and a ($\alpha_1 = 1$, $\mu_1 = -642.2$, $\alpha_2 = 2$, $\mu_2 = 791.2$, $\alpha_3 = 300$, $\mu_3 = 3.7e-9$) for

the flank region of the hemisphere. The shell was meshed with 24 axisymmetric, quadratic shell elements (SAX2). During the simulation the structure was uniformly pressurized and equilibrium strains were computed at 5 bar and 10 bar. Boundary conditions were applied to the bottom point of the rotational profile which was fixed in z-direction (i.e. axis of symmetry) but could freely move along the perpendicular x-axis.
Curves in Fig. 4C where calculated by combining Eqn.4.2, Eqn.4.2 and the relationship between hoop stress σ_h and pressure P in a thin-walled spherical pressure vessel (radius r,thickness d) (41),

$$\sigma_h = \frac{Pr}{2d}.$$

We also tested the hypothesis that the non-linearity in our expansion maps could simply be a consequence of not using a logarithmic strain measure. Therefore we investigated how a spherical shell made of incompressible, isotropic, linear (with respect to true strain) material would deform. In this case hoop stress is proportional to the true circumferential strain. We then checked how well our osmotic expansion/shrinkage measurements would fit such a linear relationship. To this end we calculated a circumferential strain (based on average shrinkage/expansion in the peripheral/central region) and inserted the result in Eqn.4.2 to retrieve hoop stresses which are equivalent to either 5 or 10 bar pressure. It turned out that a linear material model would roughly fit the peripheral region but could not account for the strain stiffening observed in the central region (Fig.S7).

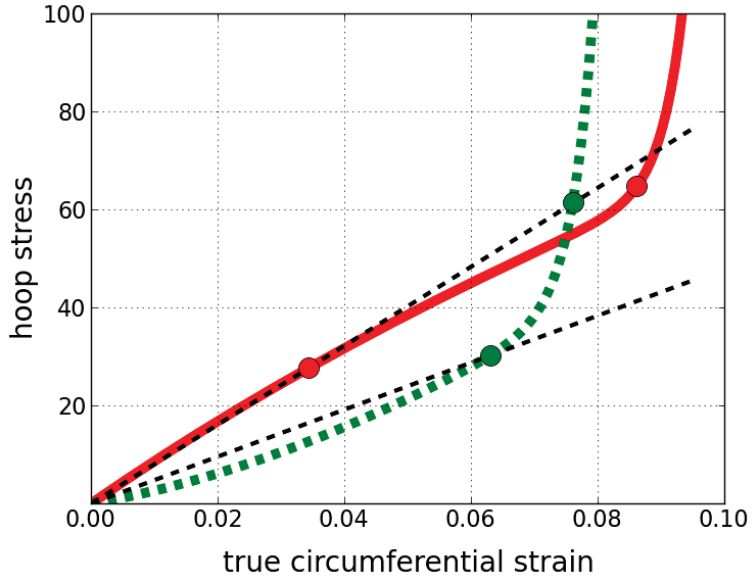

Fig. S7: **Relationship between stress and strain in a thin-walled spherical pressure vessel** Linear material models (black dashed) which fit hoop stresses at 5 bar pressure in the periphery (left red circle) and in the apical region (left green circle) compared to Ogden-hyperelastic models which fit hoop stresses at 5 bar and 10 bar (right red resp. green circle). While a linear model fits reasonably well for the peripheral region it would strongly overestimate strains in the central region of the apex at 10 bar. We define the linear regime to be the range of strains for which a linear material model provides a reasonable fit.

4.3 Effect of plasmolysis point on mechnical interpretation

We determined that the plasmolysis point of cells in the apex is somewhere between 0.3M and 0.4M. If cells plasmolyse below 0.4M, the pressure drop from 0.2M to 0.4M would be less than 5 bar. This means that in strain stiffened cells, the shrinkage occurs over a smaller pressure change than the expansion, and thus the cells would be even more strain stiffened. This can also contribute to cells showing more expansion than deflation in the cells which are not strain stiffened.

4.4 Finite element analysis on reconstructed meristem surfaces

It is well known that flat structures tend to be under higher tangential tension than curved ones if equally pressurized. In the following FE analysis we studied this effect on a shell which has a meristem geometry but homogeneous material

properties. The analysis was done in artificial units because we were interested in qualitative differences of the stress-strain distribution.

MorphoGraphX was used to extract the surface of different meristems as triangular meshes (3700-14000 vertices). Each mesh was imported into Abaqus and used to define a shell of constant thickness (approximately 0.02 of the radius of the base). We then assigned the same isotropic, linear-elastic material (dimensionless, elastic modulus = 200, Poisson ratio = 0.5) to all the meshes and specified the element type to be linear shell elements (Fig.S8). During the simulation the shell was pressurized from underneath and clamped around the area of interest.

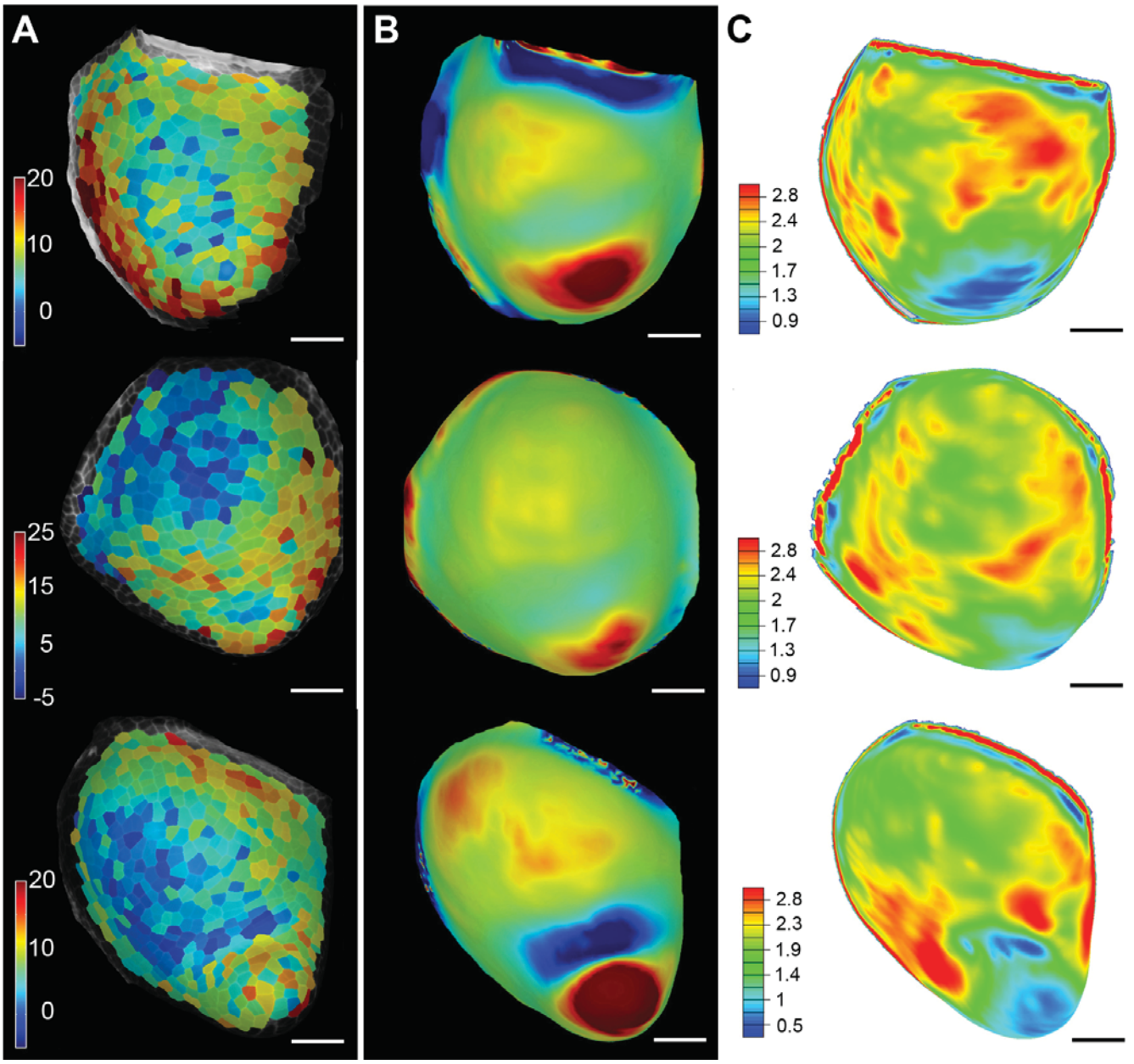

Fig. S8: **Comparison between curvature and strain distribution in a homogeneous shell.** Three different meristems are presented (A) Heat maps of cell expansion after hypo-osmotic treatment. (B) Maps of Gaussian curvature of the apex surface with red-positive, and blue-negative curvature. (C) FEM simulations of areal strain patterns. A shell of homogeneous material would mostly expand in flat areas. Colorbar (A, C): area increase in percent. Scale bars: 40 μm

5 Implications of strain stiffening material properties on experimental work

The non-linear behavior of the cell wall has important implications when doing mechanical testing in intact tissues. Since the tangential modulus depends on the level of strain applied, it is of particular importance to control osmotic conditions for a proper characterization of material properties. It seems reasonable to osmotically deflate cell in order to isolate cell wall properties from the influence of turgor pressure in micro-indentation experiments. However, strain stiffening of the cell wall may cause the cells in the central region to appear stiffer when the apex is turgid, and softer when that same apex is deflated. It is also possible that at specific pressure levels, measurements in different areas of the same meristem may yield the same result, even if the material properties are very different. This will happen if the pressure is close to the point where the tangential modulus of both materials is the same (Fig. 4C), which seems to be the case in a tomato shoot apex under normal turgor pressure.

References and Notes

1. T. Steeves, I. Sussex, Eds., *Patterns in Plant Development* (Cambrige Univ. Press, New York, 1988).

2. D. Kwiatkowska, J. Dumais, Growth and morphogenesis at the vegetative shoot apex of *Anagallis arvensis* L. *J. Exp. Bot.* **54**, 1585 (2003).

3. O. Grandjean *et al*., In vivo analysis of cell division, cell growth, and differentiation at the shoot apical meristem in *Arabidopsis*. *Plant Cell* **16**, 74 (2004).

4. G. V. Reddy, M. G. Heisler, D. W. Ehrhardt, E. M. Meyerowitz, Real-time lineage analysis reveals oriented cell divisions associated with morphogenesis at the shoot apex of *Arabidopsis thaliana*. *Development* **131**, 4225 (2004).

5. S. Vanneste, J. Friml, Auxin: A trigger for change in plant development. *Cell* **136**, 1005 (2009).

6. M. G. Heisler *et al*., Patterns of auxin transport and gene expression during primordium development revealed by live imaging of the *Arabidopsis* inflorescence meristem. *Curr. Biol.* **15**, 1899 (2005).

7. D. Reinhardt *et al*., Regulation of phyllotaxis by polar auxin transport. *Nature* **426**, 255 (2003).

8. D. L. Rayle, R. E. Cleland, The Acid Growth Theory of auxin-induced cell elongation is alive and well. *Plant Physiol.* **99**, 1271 (1992).

9. D. J. Cosgrove, Growth of the plant cell wall. *Nat. Rev. Mol. Cell Biol.* **6**, 850 (2005).

10. T. Vernoux, J. Kronenberger, O. Grandjean, P. Laufs, J. Traas, PIN-FORMED 1 regulates cell fate at the periphery of the shoot apical meristem. *Development* **127**, 5157 (2000).

11. D. Reinhardt, T. Mandel, C. Kuhlemeier, Auxin regulates the initiation and radial position of plant lateral organs. *Plant Cell* **12**, 507 (2000).

12. A. Fleming, S. McQueen-Mason, T. Mandel, C. Kuhlemeier, Induction of leaf primordia by the cell wall protein expansin. *Science* **276**, 1415 (1997).

13. S. Pien, J. Wyrzykowska, S. McQueen-Mason, C. Smart, A. Fleming, Local expression of expansin induces the entire process of leaf development and modifies leaf shape. *Proc. Natl. Acad. Sci. U.S.A.* **98**, 11812 (2001).

14. A. Peaucelle *et al*., *Arabidopsis* phyllotaxis is controlled by the methyl-esterification status of cell-wall pectins. *Curr. Biol.* **18**, 1943 (2008).

15. A. Peaucelle *et al*., Pectin-induced changes in cell wall mechanics underlie organ initiation in *Arabidopsis*. *Curr. Biol.* **21**, 1720 (2011).

16. M. G. Heisler *et al*., Alignment between PIN1 polarity and microtubule orientation in the shoot apical meristem reveals a tight coupling between morphogenesis and auxin transport. *PLoS Biol.* **8**, e1000516 (2010).

17. O. Hamant *et al*., Developmental patterning by mechanical signals in *Arabidopsis*. *Science* **322**, 1650 (2008).

18. P. Milani *et al*., *In vivo* analysis of local wall stiffness at the shoot apical meristem in Arabidopsis using atomic force microscopy. *Plant J.* **67**, 1116 (2011).

19. Materials and methods are available as supporting material on *Science* Online.

20. C. Storm, J. J. Pastore, F. C. MacKintosh, T. C. Lubensky, P. A. Janmey, Nonlinear elasticity in biological gels. *Nature* **435**, 191 (2005).

21. S. E. Whitney, M. G. Gothard, J. T. Mitchell, M. J. Gidley, Roles of cellulose and xyloglucan in determining the mechanical properties of primary plant cell walls. *Plant Physiol.* **121**, 657 (1999).

22. R. R. Vincent, D. N. Pinder, Y. Hemar, M. A. Williams, Microrheological studies reveal semiflexible networks in gels of a ubiquitous cell wall polysaccharide. *Phys. Rev. E Stat. Nonlin. Soft Matter Phys.* **76**, 031909 (2007).

23. J. Dumais, C. R. Steele, New evidence for the role of mechanical forces in the shoot apical meristem. *J. Plant Growth Regul.* **19**, 7 (2000).

24. J. M. Selker, G. L. Steucek, P. B. Green, Biophysical mechanisms for morphogenetic progressions at the shoot apex. *Dev. Biol.* **153**, 29 (1992).

25. R. Vandiver, A. Goriely, Differential growth and residual stress in cylindrical elastic structures. *Philos. Transact. A Math. Phys. Eng. Sci.* **367**, 3607 (2009).

26. V. Mirabet, P. Das, A. Boudaoud, O. Hamant, The role of mechanical forces in plant morphogenesis. *Annu. Rev. Plant Biol.* **62**, 365 (2011).

27. U. Kutschera, K. J. Niklas, The epidermal-growth-control theory of stem elongation: An old and a new perspective. *J. Plant Physiol.* **164**, 1395 (2007).

28. J. A. Lockhart, An analysis of irreversible plant cell elongation. *J. Theor. Biol.* **8**, 264 (1965).

29. T. Vernoux *et al*., The auxin signalling network translates dynamic input into robust patterning at the shoot apex. *Mol. Syst. Biol.* **7**, 508 (2011).

30. R. Sablowski, The dynamic plant stem cell niches. *Curr. Opin. Plant Biol.* **10**, 639 (2007).

31. R. K. Yadav, T. Girke, S. Pasala, M. Xie, G. V. Reddy, Gene expression map of the *Arabidopsis* shoot apical meristem stem cell niche. *Proc. Natl. Acad. Sci. U.S.A.* **106**, 4941 (2009).

32. E. Shani *et al*., Cytokinin regulates compound leaf development in tomato. *Plant Cell* **22**, 3206 (2010).

33. E. M. Bayer *et al*., Integration of transport-based models for phyllotaxis and midvein formation. *Genes Dev.* **23**, 373 (2009).

34. P. Barbier De Reuille, R. S. Smith, MorphoGraphX (2011); www.MorphoGraphX.org.

35. J. Bloomenthal, in *Graphics Gems IV*, P. Heckbert, Ed. (AP Professional, Boston, 1994), chap. IV.8, pp. 324–349.

36. P. Sieber *et al*., Transgenic Arabidopsis plants expressing a fungal cutinase show alterations in the structure and properties of the cuticle and postgenital organ fusions. *Plant Cell* **12**, 721 (2000).

37. G. Houlsby, A. Puzrin, *Principles of Hyperplasticity: An Approach to Plasticity Theory Based on Thermodynamic Principles* (Springer, London, 2006).

38. M. Snow, R. Snow, On the determination of leaves. *New Phytol.* **46**, 5 (1947).

39. G. Hussey, Mechanical stress in the shoot apices of *Euphorbia*, *Lycopersicon*, and *Pisum* under controlled turgor. *Ann. Bot. (London)* **37**, 57 (1973).

40. R. W. Ogden, Large deformation isotropic elasticity - on the correlation of theory and experiment for incompressible rubberlike solids. *Proc. R. Soc. London A Math. Phys. Sci.* **326**, 565 (1972).

41. D. Annaratone, *Pressure Vessel Design* (Springer, New York, 2007).